



CHORUS

This is the accepted manuscript made available via CHORUS. The article has been published as:

Chaotic Rayleigh-Bénard convection with finite sidewalls

M. Xu and M. R. Paul

Phys. Rev. E **98**, 012201 — Published 2 July 2018

DOI: [10.1103/PhysRevE.98.012201](https://doi.org/10.1103/PhysRevE.98.012201)

Chaotic Rayleigh-Bénard Convection with Finite Sidewalls

M. Xu and M. R. Paul*

Department of Mechanical Engineering, Virginia Tech, Blacksburg, Virginia 24061

We explore the role of finite sidewalls on chaotic Rayleigh-Bénard convection. We use large-scale parallel spectral-element numerical simulations for the precise conditions of experiment for cylindrical convection domains. We solve the Boussinesq equations for thermal convection and the conjugate heat transfer problem for the energy transfer at the solid sidewalls of the cylindrical domain. The solid sidewall of the convection domain has finite values of thickness, thermal conductivity, and thermal diffusivity. We compute the Lyapunov vectors and exponents for the entire fluid-solid coupled problem. We quantify the chaotic dynamics of convection over a range of thermal sidewall boundary conditions. We find that the dynamics become less chaotic as the thermal conductivity of the sidewalls increases as measured by the value of the fractal dimension of the dynamics. The thermal conductivity of the sidewall is a stabilizing influence, the heat transfer between the fluid and solid regions is always in the direction to reduce the fluid motion near the sidewalls. Although the heat interaction for strongly conducting sidewalls is only about 1% of the heat transfer through the fluid layer, it is sufficient to reduce the fractal dimension of the dynamics by approximately 25% in our computations.

I. INTRODUCTION

Fluid convection continues to play a central role in building our understanding of the complex dynamics that occur when spatially extended systems are driven far-from-equilibrium [1]. In particular, studies of Rayleigh-Bénard convection, the buoyancy driven convection that occurs when a shallow layer of fluid is heated uniformly from below, continues to provide fundamental new physical insights into long-standing and difficult questions in pattern formation, nonlinear dynamics, and condensed matter physics [1–3].

However, many important theoretical results [1, 2] are derived for idealized situations that are difficult, if not impossible, to reproduce in experiment. For example, periodic boundaries or the assumption of an infinite layer of fluid. Many careful and seminal experiments have been conducted in cylindrical convection domains [3, 4]. In this case, one must consider the role of the sidewalls of the domain on the fluid convection.

The onset of convection has been studied in detail for perfectly insulating and perfectly conducting sidewalls [5–8], for sidewalls with finite values of thermal conductivity [9–12], as well as for top and bottom boundaries that are poorly conducting [13]. Much of the work regarding the influence of the sidewalls has focussed upon the linear instabilities near the convective threshold for cylindrical domains of small to intermediate aspect ratios $1/2 \lesssim \Gamma \lesssim 20$ where $\Gamma = r_0/d$ with r_0 the radius of the cylindrical domain and d the depth of the fluid layer.

In particular, this work has determined the value of the critical Rayleigh number R_c and the initial pattern of convection rolls that emerge just above threshold as a function of Γ and the sidewall thermal boundary conditions. These investigations explored time-independent

dynamics and mostly considered sidewalls at the extreme conditions of being either perfectly insulating or perfectly conducting [5, 6, 8]. It was shown that the critical Rayleigh number is larger for perfectly conducting sidewalls than it is for perfectly insulating sidewalls.

In other words, conducting sidewalls are stabilizing. This is a direct result of the fact that heat is able to leave, or enter, the domain through the sidewalls for conducting sidewalls. This heat transfer is always in the direction to bring the temperature profile in the fluid region back toward the linear conduction profile. This results in the reduction of thermal gradients in the fluid near the wall. This raises the threshold for convection and results in the larger value of the critical Rayleigh number for conducting sidewalls.

In Refs. [9–12] finite values of the conductivity of the solid sidewall were explored for time-independent dynamics using a thin sidewall assumption (or fin approximation). This allowed the sidewall to be represented completely by a boundary condition on the fluid domain, and furthermore, the thermal conductivity of the sidewalls could be varied continuously over the range from perfectly insulating to perfectly conducting.

In the study presented here, we explore the time-dependent dynamics of convection far from the convective threshold $R > R_c$ for general sidewall conditions where R is the Rayleigh number. In our investigation we have sidewalls of finite thickness that are composed of a material with finite values of density, thermal conductivity, and heat capacity. We explore the influence of the sidewalls on the chaotic dynamics of convection. In order to accomplish this, we numerically solve the full conjugate heat transfer problem along with the Boussinesq equations that describe the fluid convection.

Furthermore, we simultaneously integrate many copies of the tangent space equations in order to compute the spectrum of Lyapunov vectors and exponents. We then use Lyapunov based diagnostics such the Lyapunov exponent spectrum, the fractal dimension, and the spatiotem-

* Corresponding author: mrp@vt.edu

poral dynamics of the leading order Lyapunov vector to probe the dynamics in detail as a function of finite sidewalls over a range of conditions from perfectly insulating to perfectly conducting.

The paper is organized as follows. In §II we describe our general approach to investigate Rayleigh-Bénard convection in a cylindrical domain with finite sidewalls. We describe the Boussinesq equations and the full conjugate heat transfer problem of interest. Lastly, we describe how we compute the Lyapunov vectors and exponents. In §III we present the results of our computations and discuss the new physical insights we have gained. We first discuss the dynamics and the patterns we find. We quantify and explore the relevant heat transfers in the problem and use the Lyapunov exponents and leading order Lyapunov vector to quantify the variation in the chaotic dynamics as a function of the sidewalls. In §IV we present some concluding remarks.

II. APPROACH

A. Rayleigh-Bénard Convection

We will use the configuration shown in Fig. 1 to describe Rayleigh-Bénard convection with finite sidewalls. The fluid is contained in the cylindrical region $r^* \leq r_1$ where r^* is the dimensional radial coordinate whose origin is at the center of the domain. The annular region $r_1 < r^* \leq r_2$ is composed entirely of a solid material, we will refer to this as the sidewall of the domain. In order to clearly distinguish between fluid and solid properties, we will use a subscript f on fluid properties, and a subscript s on solid properties. The vertical thickness of the domain everywhere is d . The domain is oriented such that gravity is pointing downward in Fig. 1(a).

The hot bottom surface and cold top surface are composed of a perfectly conducting material over the entire domain $r^* \leq r_2$. The bottom surface is held at a constant temperature T_h , the top surface is held at a constant cold temperature T_c , and we will refer to their difference as $\Delta T = T_h - T_c$. Lastly, we will assume the entire apparatus is placed in a poorly conducting environment for $r^* > r_2$, such that the outside boundary condition on the sidewalls at $r^* = r_2$ is perfectly insulating.

Using these conventions, the aspect ratio of the fluid filled portion of the domain is $\Gamma_1 = r_1/d$ and the aspect ratio of the entire domain is $\Gamma_2 = r_2/d$. In all of our calculations we have used $\Gamma_1 = 10$ and $\Gamma_2 = 15$.

The Boussinesq equations [1] govern the fluid motion and represent the conservation of momentum, energy, and mass in the fluid. In nondimensional form these

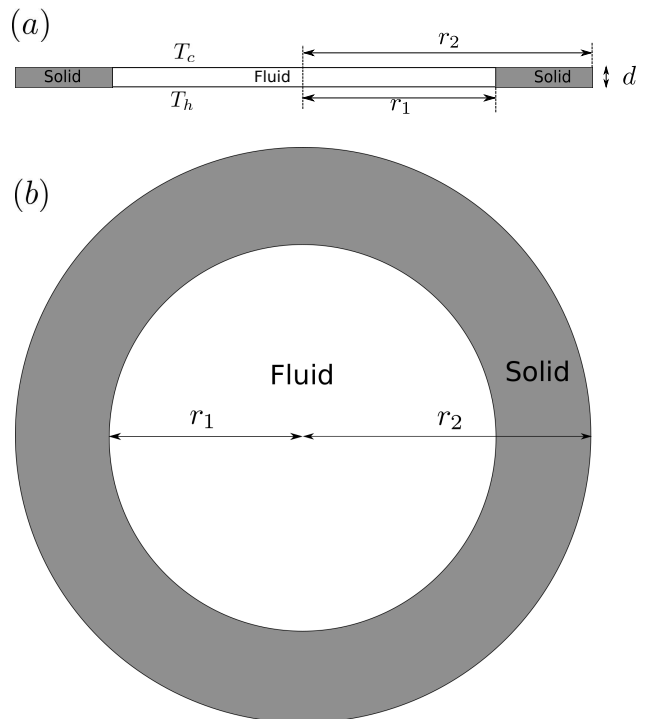


FIG. 1. A schematic of the cylindrical convection domain used in the numerical simulations. (a) A vertical cross-section through the domain showing the r^*-z^* plane. This projection clearly shows the depth d of the layer, the radius of the region containing the fluid r_1 , and the outer radius of the solid sidewall r_2 . The solid sidewall is grey and the fluid filled region is white. The bottom surface is hot at temperature T_h and the top surface is cold at temperature T_c . (b) A projection of the domain in the x^*-y^* or $r^*-\theta$ plane. Panels (a) and (b) are drawn to scale. In our notation, a superscript $*$ indicates a coordinate in dimensional form.

equations are

$$\sigma^{-1} \left(\frac{\partial \vec{u}}{\partial t} + \vec{u} \cdot \nabla \vec{u} \right) = -\nabla p + \nabla^2 \vec{u} + RT_f \hat{z} \quad (1)$$

$$\frac{\partial T_f}{\partial t} + \vec{u} \cdot \nabla T_f = \nabla^2 T_f \quad (2)$$

$$\nabla \cdot \vec{u} = 0 \quad (3)$$

where \vec{u} is the fluid velocity vector, p is the pressure, T_f is the temperature, and \hat{z} is a unit vector in the vertical direction opposing gravity.

We have followed the often used convention for Rayleigh-Bénard convection in choosing our scales for the nondimensionalization [14]. We use the depth d of the domain as the length scale, the diffusion time for heat in the fluid d^2/α_f for the time scale where α_f is the thermal diffusivity of the fluid, and the constant temperature difference ΔT between the hot bottom plate and cold top plate as the temperature scale.

We use the no-slip boundary condition such that $\vec{u} = 0$ at all solid surfaces in contact with the fluid. The top and bottom plates are held at a constant temperature

which is equivalent to assuming these surfaces are perfectly conducting. In our notation this can be expressed as $T_f(z=0) = 1$ and $T_f(z=1) = 0$.

The Prandtl number σ and Rayleigh number R are the important nondimensional parameters that appear in Eqs. (1)-(3). The Prandtl number $\sigma = \nu_f/\alpha_f$ represents the ratio between the diffusion of momentum and heat in the fluid where ν_f is the kinematic viscosity of the fluid. The Prandtl number for solar convection $\sigma \sim 10^{-7}$, for air or the compressed gases often used in experiment $\sigma \sim 1$, for water $\sigma \sim 7$, and for the convection in the earth's mantle $\sigma \sim 10^{23}$. In our study we will use $\sigma = 1$ which aligns well with many compressed gas experiments (c.f. [3]).

The Rayleigh number

$$R = \frac{\beta_f g \Delta T d^3}{\alpha_f \nu_f} \quad (4)$$

represents the ratio of buoyancy to dissipation where β_f is the coefficient of thermal expansion for the fluid and g is the acceleration due to gravity. For an infinite layer of fluid, the critical Rayleigh number for the onset of convection is $R_c = 1707.76$ [15]. For cylindrical domains with large aspect ratios $\Gamma \gtrsim 10$, as the Rayleigh number is increased the convection rolls become time dependent $R \approx 2000$, chaotic $R \approx 5000$, and then eventually turbulent $R \gtrsim 30000$.

B. Conjugate Problem

The nondimensional equation representing the conservation of energy in the region containing the solid sidewalls $\Gamma_1 \leq r \leq \Gamma_2$ is

$$\frac{\partial T_s}{\partial t} = \beta_\alpha \nabla^2 T_s \quad (5)$$

where r is the nondimensional radial coordinate and T_s is the temperature of the solid. We have used the same scales for the nondimensionalization of Eq. (5) that we used in the fluid equations Eqs. (1)-(3). The nondimensional term

$$\beta_\alpha = \frac{\alpha_s}{\alpha_f} \quad (6)$$

represents the ratio of the thermal diffusivities of the solid and fluid.

The boundary conditions for each of the surfaces of the solid sidewalls must be specified. We again assume that the top and bottom surfaces are perfect conductors such that the temperature at these surfaces remain constant. This can be expressed as $T_s(z=0) = 1$ and $T_s(z=1) = 0$ for $\Gamma_1 \leq r \leq \Gamma_2$. We assume that the entire apparatus is placed in a poorly conducting environment such that it is perfectly insulating which can be expressed as $\nabla \cdot T_s \hat{n} = 0$ where \hat{n} is an outward pointing unit normal. For our

geometry this reduces to

$$\left. \frac{\partial T_s}{\partial r} \right|_{r=\Gamma_2} = 0. \quad (7)$$

The coupling between the fluid and solid regions occurs via the thermal boundary condition at the sidewall. This boundary condition at the fluid-solid interface is

$$\left. \frac{\partial T_f}{\partial r} \right|_{r=\Gamma_1} = \beta_k \left. \frac{\partial T_s}{\partial r} \right|_{r=\Gamma_1} \quad (8)$$

where

$$\beta_k = \frac{k_s}{k_f} \quad (9)$$

is the ratio of the thermal conductivities of the solid material and of the fluid.

The conjugate heat transfer problem has a vast parameter space in terms of β_k and β_α . For example, many modern research experiments on Rayleigh-Bénard convection use a compressed gas such as sulfur hexafluoride (SF_6) in a domain with sidewalls made with a thermoplastic such as polyethersulfone. For this particular combination of SF_6 and polyethersulfone, $\beta_k \approx 10$ and $\beta_\alpha \approx 0.6$. However, for water and steel the result is $\beta_k \approx 386$ and $\beta_\alpha \approx 112$ and if we replace the sidewalls with a hard rubber and keep water as the fluid we have $\beta_k \approx 0.2$ and $\beta_\alpha \approx 0.4$ (c.f. [16] for material properties).

It is not our intention to explore this large parameter space, but rather to investigate the chaotic dynamics of convection as the conductivity of the sidewalls changes over the range from perfectly insulating to perfectly conducting. In light of this, we note that β_α can be expressed as

$$\beta_\alpha = \frac{\beta_k}{\beta_{\rho c_p}} \quad (10)$$

where

$$\beta_{\rho c_p} = \frac{(\rho c_p)_s}{(\rho c_p)_f}. \quad (11)$$

In our study, we will assume $\beta_{\rho c_p} = 1$ and we will vary β_k from small to large values. For many, but not all, combinations of fluid and solid $\beta_{\rho c_p} \sim \mathcal{O}(1)$ such that this would be a reasonable approximation. More importantly, this allows us to explore the role of the sidewalls on chaotic convection by varying only the single parameter β_k . We note that $\beta_k = \beta_\alpha$ for our assumption of $\beta_{\rho c_p} = 1$. Therefore, when we increase or decrease β_k we are also increasing or decreasing β_α . We would also like to point out that the assumption $(\rho c_p)_s = (\rho c_p)_f$ yields the following expression for the ratio of the thermal masses of the solid sidewall and fluid regions

$$\frac{(m c_p)_s}{(m c_p)_f} = \left(\frac{\Gamma_2}{\Gamma_1} \right)^2 - 1 \quad (12)$$

where m is the mass. Using our values for Γ_1 and Γ_2 yields $(mc_p)_s/(mc_p)_f = 1.25$ indicating that the sidewall is an effective thermal boundary.

We emphasize that our numerical solution is for the complete transient dynamics of the conjugate problem with sidewalls that have finite values of thickness, thermal conductivity, heat capacity, and density. We have not made any approximations such as a fin approximation which has often been done in the past [9–12].

When using the fin approximation, one assumes that the solid region is very thin in the radial direction, $r_2 - r_1 \ll r_1$ which simplifies the analysis significantly. In this case, the radial temperature profile in the solid is assumed to be a constant at any time t , and the temperature in the solid then reacts instantaneously with changes in the fluid temperature. Mathematically, this is equivalent to setting $\beta_{\rho c_p} = 0$ and neglecting radial derivatives in Eq. (5). As a result, the contribution of the solid region can be captured entirely by the boundary condition Eq. (8) and one then only needs to solve the fluid equations with the appropriate boundary conditions.

There are many important applications where this approximation is useful and justified, such as the thin walls often associated with solar collectors. However, our main interest here is to probe the dynamics in the absence of idealizations such as this and to build our physical understanding of the complex dynamics of the conjugate problem when these finite properties of the sidewalls are important. With this in mind we have chosen our parameters to be relevant for the conditions that are often the case for experimental investigations of Rayleigh-Bénard convection [1, 3].

C. Lyapunov Vectors and Exponents

In order to quantify the chaotic dynamics we also compute the spectrum of Lyapunov vectors and exponents (c.f. [17, 18]) for the full conjugate problem described by Eqs. (1)-(3) and (5). The general approach we use for computing the Lyapunov vectors can be found in Ref. [19, 20]. In the following we present only the essential details that are needed to describe our computations.

The Lyapunov vectors and exponents arise naturally when treating the conjugate problem as a dynamical system. In this approach, the state of the fluid-solid system at any particular instance of time is represented as a single point in an infinite dimensional state space. The time variation of the system results in an orbit or trajectory through this state space.

By discretizing the problem in order to perform a numerical simulation this state space is no longer of infinite dimension but is very high-dimensional. In our numerical representation, the state space is the collection of all of the values of velocity, temperature, and pressure at every grid point. For the computations presented here, the dimension of the state space for the numerics is on

the order of $\sim 10^6$.

At every point in the state space, one can compute the rate of growth or decay of a small perturbation to the dependent variables in all possible directions. For infinitesimal perturbations, this is given by the tangent space equations. The tangent space equations are the linearization of the complete equations that describe the dynamics of these small perturbations. For the fluid portion of the domain, the tangent space equations are

$$\sigma^{-1} \left(\frac{\partial}{\partial t} \delta \vec{u}^{(i)} + \vec{u} \cdot \nabla \delta \vec{u}^{(i)} + \delta \vec{u}^{(i)} \cdot \nabla \vec{u} \right) = -\nabla \delta p^{(i)} + \nabla^2 \delta \vec{u}^{(i)} + R \delta T_f^{(i)} \hat{z} \quad (13)$$

$$\frac{\partial}{\partial t} \delta T_f^{(i)} + \vec{u} \cdot \nabla \delta T_f^{(i)} + \delta \vec{u}^{(i)} \cdot \nabla T_f = \nabla^2 \delta T_f^{(i)} \quad (14)$$

$$\nabla \cdot \delta \vec{u}^{(i)} = 0 \quad (15)$$

where $\delta \vec{u}^{(i)}$, $\delta T_f^{(i)}$, and $\delta p^{(i)}$ are the i th perturbation to the fluid velocity, temperature, and pressure. In our notation $i = 1, 2, \dots, N_\lambda$ where N_λ is the total number of Lyapunov exponents and vectors that one would like to compute.

The perturbation velocity vanishes at all solid surfaces because of the no-slip boundary condition to yield

$$\delta \vec{u}^{(i)} = 0. \quad (16)$$

The temperature perturbation also vanishes at the top and bottom plates because they are perfectly conducting which yields

$$\delta T_f(z=0)^{(i)} = \delta T_f(z=1)^{(i)} = 0 \quad (17)$$

for $r \leq \Gamma_1$.

In a similar fashion, the tangent space equation for the solid sidewall region can be expressed as

$$\frac{\partial}{\partial t} \delta T_s^{(i)} = \beta_\alpha \nabla^2 \delta T_s^{(i)} \quad (18)$$

where $\delta T_s^{(i)}$ is the i th perturbation of the temperature in the solid sidewall region. The top and bottom surfaces in this region are also perfectly conducting which yields

$$\delta T_s(z=0)^{(i)} = \delta T_s(z=1)^{(i)} = 0 \quad (19)$$

for $\Gamma_1 \leq r \leq \Gamma_2$. The perfectly insulating outer sidewall yields

$$\frac{\partial}{\partial r} \delta T_s^{(i)} \Big|_{r=\Gamma_2} = 0. \quad (20)$$

Lastly, the boundary condition at the sidewall interface between the fluid and solid is

$$\frac{\partial}{\partial r} \delta T_f^{(i)} \Big|_{r=\Gamma_1} = \beta_k \frac{\partial}{\partial r} \delta T_s^{(i)} \Big|_{r=\Gamma_1}. \quad (21)$$

The tangent space equations can be expressed more compactly as

$$\frac{d\delta \mathbf{H}^{(i)}(t)}{dt} = \mathbf{J}[\mathbf{H}(t)] \delta \mathbf{H}^{(i)}(t) \quad (22)$$

where $\mathbf{H}(t) = [\bar{u}(t), T(t)]$ and $\delta\mathbf{H}^{(i)}(t) = [\delta\bar{u}^{(i)}(t), \delta T^{(i)}(t)]$. Both $\mathbf{H}(t)$ and $\delta\mathbf{H}^{(i)}(t)$ are large $4 \times N$ matrices where N is the number of grid points used to resolve the entire fluid-solid domain. In Eq. (22), \mathbf{J} is the Jacobian of Eqs. (1)-(3) and (5) evaluated at time t .

The perturbations are reorthonormalized periodically in time using a Gram-Schmidt procedure which yields a value of the magnitude for each Lyapunov vector $\|\delta\mathbf{H}^{(i)}(t_N)\|$ where t_N represents the amount of time between reorthonormalizations. In our simulations we have used $t_N = 0.01$ (this corresponds with every 10 steps where we have used $\Delta t = 0.001$). The exponential growth or decay that occurred over the time interval t_N yields what are often called the spectrum of instantaneous Lyapunov exponents $\tilde{\lambda}_i$. The long-time average of $\tilde{\lambda}_i$ converges to the spectrum of Lyapunov exponents λ_i .

Given the spectrum of Lyapunov exponents λ_i , the Kaplan-Yorke formula [21] provides an estimate for the fractal dimension D_λ of the dynamics

$$D_\lambda = j + \frac{\sum_{i=1}^n \lambda_i}{|\lambda_{j+1}|} \quad (23)$$

where j is the largest integer n such that summation in the numerator is positive. The fractal dimension D_λ provides an estimate for the number of active chaotic degrees of freedom, on average [22].

III. RESULTS AND DISCUSSION

We have conducted numerical simulations of the full conjugate heat transfer problem of chaotic Rayleigh-Bénard convection for a range of parameters. Figure 1 illustrates the details of our geometry and the conventions used in our description. In all of our calculations, the Rayleigh number $R = 5000$, the Prandtl number $\sigma = 1$, the aspect ratio of the fluid filled region $\Gamma_1 = 10$, the aspect ratio of the entire domain including the solid sidewall $\Gamma_2 = 15$, and the heat capacity ratio $\beta_{\rho c_p} = 1$.

In order to explore the influence of the sidewall we have performed numerical simulations for $0 \leq \beta_k \leq \infty$ where $\beta_k = 0$ is a perfectly insulating sidewall, $\beta_k = \infty$ is a perfectly conducting sidewall, and values of β_k between these extremes represent a sidewall of finite thermal conductivity.

A. The heat transfer interactions for no-flow

For $R < R_c$, the fluid layer is below the convective threshold and the fluid velocity is zero everywhere. In the absence of any fluid flow $\bar{u} = 0$, the temperature profile in both the fluid filled region and in the sidewalls is the linear profile

$$T_{\text{cond}}(z) = 1 - z \quad (24)$$

due to heat conduction from the hot bottom plate to the cold top plate. This linear conduction profile is time-independent and independent of material properties. Therefore the no flow case is independent of the sidewall conductivity ratio β_k .

The spatiotemporal variation of the nondimensional heat flux $q(\vec{\xi}, t)$ at each surface of interest is given by Fourier's law of heat conduction where $\vec{\xi}$ are the coordinates of the surface and q is the heat flux normal to the surface. For the bottom and top surfaces this yields

$$q_b(x, y, t) = -\frac{\partial T_f}{\partial z} \Big|_{z=0}, \quad (25)$$

$$q_t(x, y, t) = \frac{\partial T_f}{\partial z} \Big|_{z=1} \quad (26)$$

where we have used the quantity $k_f \Delta T / d$ as the heat scale. We have chosen the signs such that heat entering the fluid domain is positive and heat leaving the fluid domain is negative. Therefore, in our notation, $q_b > 0$ since heat can only enter the fluid domain from the perfectly conducting hot bottom surface. Similarly, $q_t < 0$ since heat can only exit the fluid domain at the perfectly conducting cold top surface. For the no-flow case $T_f(z) = T_{\text{cond}}(z)$ which yields $q_b = 1$ and $q_t = -1$.

The corresponding expression for the heat flux at the sidewall interface between the fluid and solid is

$$q_w(z, \theta, t) = \frac{\partial T_f}{\partial r} \Big|_{r=\Gamma_1} \quad (27)$$

where in this case it is more convenient to use the cylindrical coordinates (r, θ, z) and again the sign is chosen such that heat entering the fluid region from the sidewall would have a positive value of the wall heat flux. For the no-flow case $q_w = 0$. However, in general, the heat flux at the sidewall can be either positive or negative.

The total amount of heat transfer through any surface of area A is just the integral of the heat flux

$$Q(t) = \int_A q dA \quad (28)$$

where we will use $Q_b(t)$, $Q_t(t)$, and $Q_w(t)$ as the total heat transfer at the bottom, top, and sidewall surfaces, respectively. For the no flow case, these expressions yield $Q_b = \pi\Gamma_1^2$, $Q_t = -\pi\Gamma_1^2$ and $Q_w = 0$ which are all constants.

The nondimensional Nusselt number Nu is often used to quantify the heat transfer in Rayleigh-Bénard convection. The Nusselt number is the ratio of heat transfer by thermal convection to the amount of heat transfer that would occur by conduction alone in the absence of convection. Using our notation, we can express the Nusselt number evaluated at the bottom and top surfaces in contact with the fluid as

$$Nu_b(t) = \frac{Q_b(t)}{\pi\Gamma_1^2} = q_b(t), \quad (29)$$

$$Nu_t(t) = \frac{|Q_t(t)|}{\pi\Gamma_1^2} = |q_t(t)|. \quad (30)$$

For the no flow case this yields $Nu_b = Nu_t = 1$.

B. The heat transfer interactions for chaotic convection

We next consider the heat transfer interactions for $R = 5000$ which yields chaotic fluid convection. We first discuss the case of a perfectly insulating sidewall boundary such that $\beta_k = 0$. In this case, we do not need to solve the full conjugate heat transfer problem since the insulating boundary can be represented as a no flux boundary condition for the heat transfer.

A typical flow field pattern for chaotic convection with a perfectly insulating sidewall is shown in Fig. 2(a). The color contours are the temperature at the horizontal mid-plane $T_f(x, y, z = 1/2, t_0)$ shown at time t_0 . Red is hot rising fluid and blue is cold falling fluid. Fig. 2(b) illustrates a typical pattern for the case of perfectly conducting sidewalls.

The general features of the flow fields shown in Fig. 2 are quite similar except where the convection rolls approach the lateral sidewalls. For the perfectly conducting sidewall there are radial temperature gradients near the sidewall that are not present in the flow field with a perfectly insulating sidewall. This is evident by the thin green region near the sidewall in Fig. 2(b).

An energy balance of the fluid filled region can be expressed as

$$\frac{d\mathcal{E}}{dt} = Q_b(t) + Q_t(t) + Q_w(t) \quad (31)$$

where $d\mathcal{E}/dt$ is the time rate of change of the energy of the fluid. For a perfectly insulating sidewall $Q_w = 0$, and all of the heat that enters the fluid layer through the bottom surface must eventually exit through the top surface. However, both $Q_b(t)$ and $Q_t(t)$ are functions of time that depend upon the patterns and dynamics of the convection rolls.

Figure 3(a) shows the time variation of $Q_b(t)$ and $|Q_t(t)|$ through the fluid layer. In general, the heat transfer through the fluid layer decreases in the presence of defects in the structure of the convection rolls and it increases when a defect structure is annihilated (c.f. [23–25]). In our problem, the aspect ratio is large enough such that at any time there are multiple defect events occurring in the flow field which adds to the complexity of the time variation of the heat transfer through the fluid layer. The axis on the right side of Fig. 3(a) shows the variation of the heat transfer as measured by the Nusselt number. The long-time average of the Nusselt number for these dynamics is $\langle \text{Nu} \rangle \approx 1.93$ where the angle brackets indicate an average over time.

This is a sustained nonequilibrium state where the long-time average of the energy change $\langle d\mathcal{E}/dt \rangle = 0$. Therefore, the long-time average of the heat flux through the bottom and top are equal such that $\langle Q_b \rangle = \langle |Q_t| \rangle$. However, it is important to point out that $d\mathcal{E}/dt \neq 0$ although it is quite small and quite insensitive to the value of β_k . In Fig. 3(b) we show the time variation of Q_{bt}

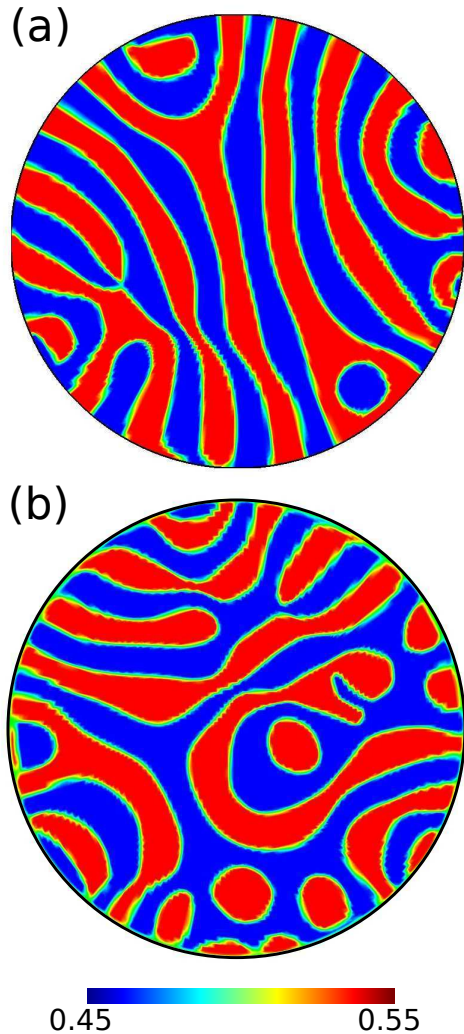


FIG. 2. (color online) Typical flow field patterns of chaotic Rayleigh-Bénard convection for (a) perfectly insulating sidewalls $\beta_k = 0$ and (b) perfectly conducting sidewalls $\beta_k = \infty$. The solid black line marks the location of the sidewall boundary. The color contours are of the temperature field at the horizontal mid-plane ($z = 1/2$) where red is hot rising fluid and blue is cold falling fluid. For perfectly insulating or perfectly conducting sidewalls the sidewall is represented as a boundary condition and we do not need to solve the conjugate heat transfer problem.

where

$$Q_{bt} = Q_b + Q_t. \quad (32)$$

For insulating sidewalls $Q_{bt} = d\mathcal{E}/dt$ by Eq. (31). For the duration of our calculation the long-time average of the energy change is $\langle d\mathcal{E}/dt \rangle = 5.2 \times 10^{-3} \approx 0$ where the standard deviation of the fluctuations is $\delta(d\mathcal{E}/dt) = 0.25$.

We next consider how the dynamics are affected by a finite sidewall with a finite value of the thermal con-

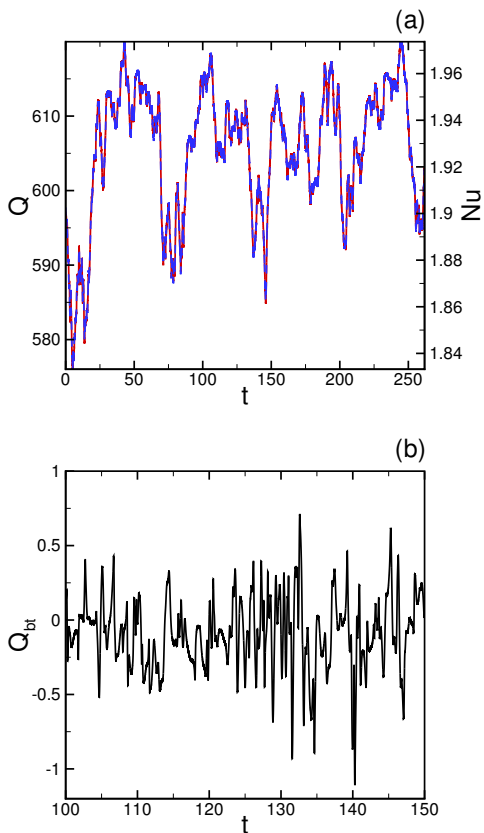


FIG. 3. (color online) The time variation of the heat transfer through the fluid layer for perfectly insulating sidewalls $\beta_k = 0$. (a) The heat transfer through the bottom plate $Q_b(t)$ (red, solid) and the heat transfer through the top plate $|Q_t(t)|$ (blue, dashed). The axis on the right shows these heat transfers as measured by the Nusselt numbers $Nu_b(t)$ and $Nu_t(t)$, respectively. The long-time average of the Nusselt number is $\langle Nu \rangle \approx 1.93$. (b) The time variation of $Q_{bt}(t)$. For an insulating sidewall $Q_{bt} = d\mathcal{E}/dt$ from Eq. (31). The long-time average from our numerical simulation is $\langle d\mathcal{E}/dt \rangle = 5.2 \times 10^{-3} \approx 0$ and the standard deviation of the fluctuations is $\delta(d\mathcal{E}/dt) = 0.25$.

ductivity ratio $\beta_k > 0$. In particular, for finite sidewalls, we have explored the dynamics at the following five values of the thermal conductivity ratio $\beta_k = \{0.01, 0.1, 1, 10, 100\}$. For finite sidewalls, the sidewall heat interactions $Q_w(t) \neq 0$ and we are interested in understanding how this affects the chaotic dynamics.

In Fig. 4 we show the time variation of $d\mathcal{E}/dt$ for several representative values of the thermal conductivity ratio. The solid (red) line is for a strongly insulating sidewall with $\beta_k = 0.01$, the dashed (blue) line is for the case when the fluid and sidewall are matched $\beta_k = 1$, and the dash-dotted (green) line is for a strongly conducting sidewall with $\beta_k = 100$.

We have computed the value of $d\mathcal{E}/dt$ using Eq. (31) by numerically evaluating the heat fluxes through the bot-

tom, top, and sidewalls. For all values of β_k we find that $d\mathcal{E}/dt$ is small. The long-time average $\langle d\mathcal{E}/dt \rangle \approx 0$ and the standard deviation of the fluctuations are $\delta(d\mathcal{E}/dt) \approx 0.25$. In light of this, we will explore the time variations of the heat transfer at the walls quantified by $Q_b(t)$, $Q_t(t)$, and $Q_w(t)$.

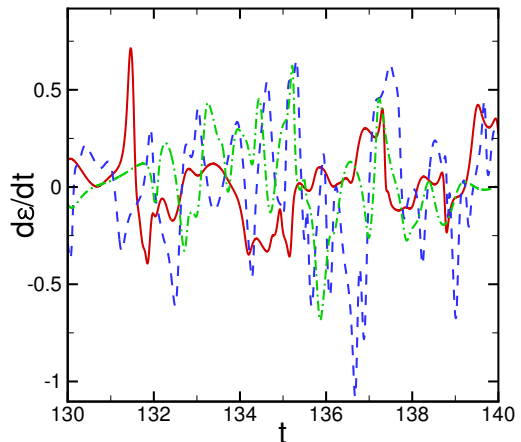


FIG. 4. (color online) The time variation of $d\mathcal{E}/dt$ as a function of the thermal conductivity ratio β_k for chaotic convection with finite sidewalls. Curves are shown for three representative cases: $\beta_k = 0.01$ (red, solid), $\beta_k = 1$ (blue, dashed), and $\beta_k = 100$ (green, dash-dotted). $d\mathcal{E}/dt$ is computed using Eq. (31) by numerically evaluating Q_b , Q_t , and Q_w . For all values of β_k the values of $d\mathcal{E}/dt$ are similar to the results shown here where the long-time average $\langle d\mathcal{E}/dt \rangle \approx 0$ and the standard deviation of the fluctuations is $\delta(d\mathcal{E}/dt) \approx 0.25$.

For finite sidewalls it is interesting to compare the time variations of $Q_{bt}(t)$ and $Q_w(t)$. In Fig. 5 we show the time variation of Q_{bt} (solid line, blue) and Q_w (dashed line, red) as a function of the thermal conductivity ratio β_k . When $Q_{bt} > 0$ this indicates that more heat has entered into the fluid layer from the hot bottom plate than the amount of heat that has left through the sidewall and cold top plate. Similarly, when $Q_{bt} < 0$, more heat has left through the top plate than has entered through the sidewall and hot bottom plate. In addition, when $Q_w > 0$ this indicates that heat is entering the fluid domain through the sidewalls at this time and similarly when $Q_w < 0$ heat is leaving the fluid domain through the sidewalls. Figure 5 shows an interesting interplay that occurs between $Q_{bt}(t)$ and $Q_w(t)$ which we discuss further.

Figure 5(a) is representative of what occurs for strongly insulating sidewalls. First, the magnitudes of $Q_{bt}(t)$ and $Q_w(t)$ are small as expected. This is because most of the heat travels through the fluid layer from the bottom to the top since there will only be a small amount of heat interactions with the sidewalls because they are strongly insulating. However, whenever there

is excess heat in the fluid $Q_{bt}(t) > 0$ we find that heat leaves through the sidewall $Q_w(t) < 0$. Similarly, whenever more heat left through the top than entered through the bottom $Q_{bt}(t) < 0$ heat enters from the sidewalls $Q_w(t) > 0$.

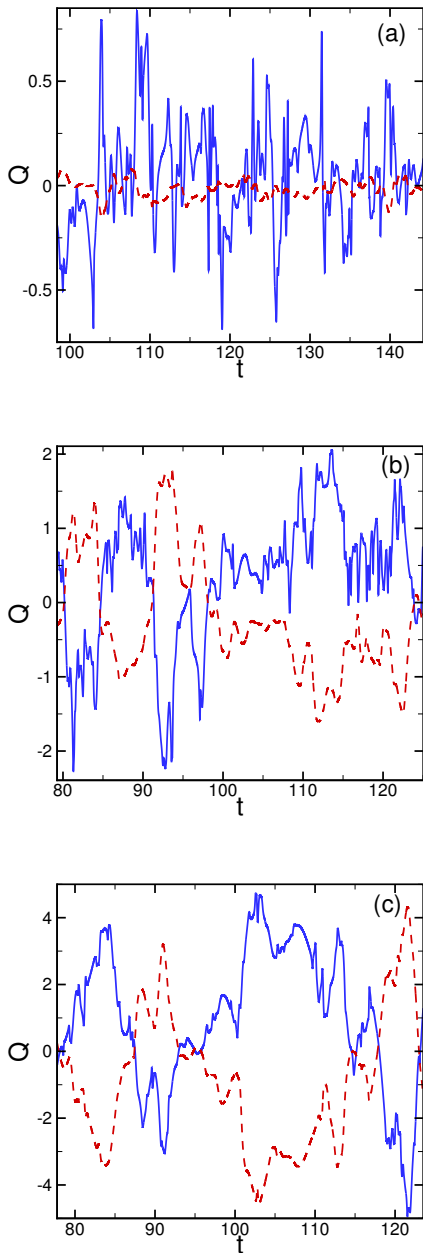


FIG. 5. (color online) The time variation of the heat transfer through the bottom, top and sidewalls for chaotic convection as a function of the thermal conductivity ratio β_k . The solid (blue) line is $Q_{bt}(t)$ and the dashed (red) line is $Q_w(t)$. (a) $\beta_k = 0.01$, (b) $\beta_k = 1$, and (c) $\beta_k = 100$.

In essence, the sidewall is a reservoir that will provide heat to, or absorb heat from, the fluid depending upon

the sign of $Q_{bt}(t)$. The result is that the sidewall heat interactions always act to stabilize the flow. The sidewall heat transfer always drives the fluid temperature back toward the perfectly conducting profile. In Fig. 5 (a) the sidewall is strongly insulating and, as a result, it is not able to provide a significant amount of heat through its interactions. As a result, the magnitude of $Q_w(t)$ always remains smaller than that of $Q_{bt}(t)$.

These trends continue and become more significant as the value of the thermal conductivity ratio increases. Figure 5(b) illustrates these heat interactions for the case when the fluid and solid sidewalls are thermally matched with $\beta_k = 1$. Again, the stabilizing effect of the heat transfer through the sidewalls results in $Q_w(t)$ mirroring Q_{bt} . In this case, the amount of heat transfer through the sidewalls is much larger than what is shown in Fig. 5(a) yet its magnitude is still smaller than that of Q_{bt} .

Figure 5(c) shows the heat transfer interactions for a strongly conducting sidewall with $\beta_k = 100$. In this case, the sidewall is able to nearly balance the heat transfer through the fluid layer from bottom to top resulting in $|Q_{bt}| \approx |Q_w|$. The stabilizing effect of the sidewalls is now at its strongest.

The results we have discussed so far have been based upon integrated quantities over the entire bottom, top, and sidewall surfaces. We next discuss in more detail the spatiotemporal variations of the flow field patterns and the heat transfer interactions. Typical flow field images from our numerical simulations are shown in Fig. 6 for the three different values of sidewall conductivity ratio of $\beta_k = \{0.1, 1.0, 10\}$. The color contours represent the temperature at the horizontal mid-plane at a particular instant of time t_0 using $T_f(x, y, z = 1/2, t_0)$ for $r \leq \Gamma_1$ and $T_s(x, y, z = 1/2, t_0)$ for $r > \Gamma_1$.

In the fluid filled region, red is hot rising fluid and blue is cold falling fluid. In the sidewall region, red is where the solid is hot and blue is where the solid is cold. In both regions green indicates a value of temperature $T_f = T_s = 1/2$ which is equivalent to the value of the linear conduction temperature at the mid-plane $T_{\text{cond}}(z = 1/2)$. We have also included a black contour line at the fluid-solid interface to clearly indicate the interface between the fluid filled and solid sidewall regions.

In Fig. 6(a), $\beta_k = 0.1$ and the sidewall is insulating relative to the fluid. For this case, there are temperature variations that extend into the solid sidewall. However, there is very little heat transfer between the fluid and sidewall regions due to the small value of the thermal conductivity of the sidewall.

Figure 6(b) shows the convective pattern for $\beta_k = 1$ which indicates that the thermal conductivity of the fluid and solid regions are exactly matched. For this case, there are again temperature variations apparent in the solid region. In addition, there is now more heat transfer interactions between the sidewall and fluid.

Lastly, in Fig. 6(c) $\beta_k = 10$ which represents a case where the sidewall is a good conductor. For this case, there is very little variation of the temperature in the

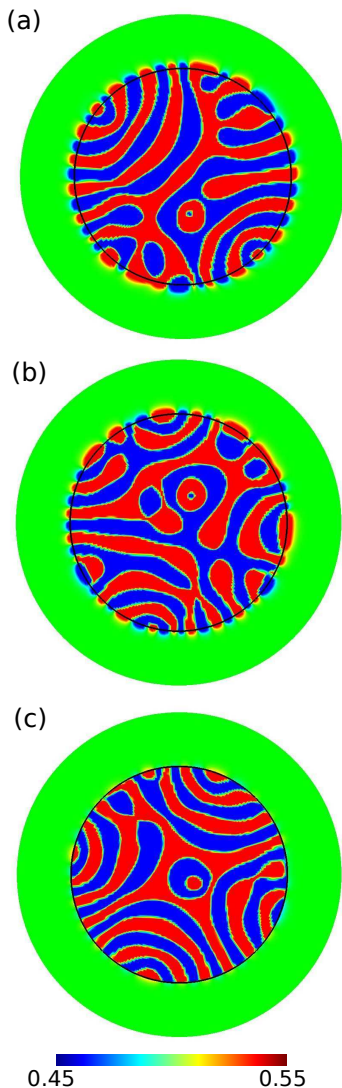


FIG. 6. Typical flow field patterns of chaotic Rayleigh-Bénard convection for three domains with different values of the thermal conductivity ratio β_k where (a) $\beta_k = 0.1$, (b) $\beta_k = 1.0$, (c) $\beta_k = 10$. From top to bottom the sidewalls go from insulating to conducting relative to the fluid. The solid black line marks the location of fluid-solid boundary. For the fluid region, the color contours of the temperature field at the horizontal mid-plane ($z = 1/2$) are shown where red is hot rising fluid and blue is cold falling fluid. For the solid region, red is a hot region and blue is a cold region.

solid region. In fact, the temperature profile at the fluid-solid interface remains nearly equal to $T_{\text{cond}}(z)$. As a result of the higher conductivity of the sidewall, and the larger thermal gradients in the fluid temperature near the sidewall, there is now more heat transfer between the fluid and sidewall.

More insight can be gained by visualizing the temperature field in the $r-z$ plane near the fluid-solid interface. This is shown in Fig. 7 for the same conditions and flow fields that are illustrated in Fig. 6. The color contours

are of the temperature field and a black vertical line is included to identify the location of the fluid-solid interface. In this representation, the linear conduction temperature profile would be a uniform change from red to blue as one goes from the bottom plate to the top plate. The linear conduction profile can be seen in Fig. 7 at the far left edge of each panel as one moves away from the sidewall interface and toward the perfectly insulating outer boundary at $r = \Gamma_2$ (not shown).

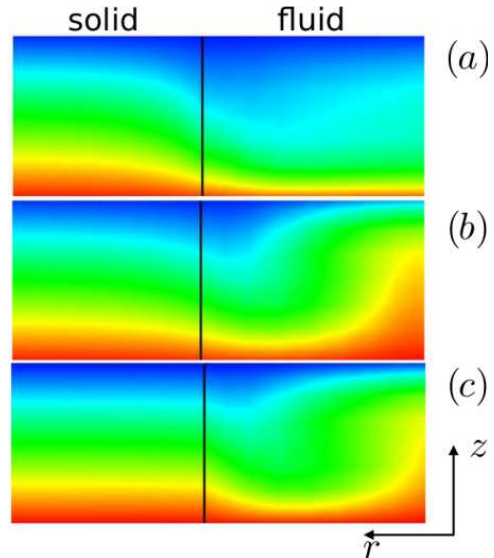


FIG. 7. Typical flow fields for $\beta_k = \{0.1, 1, 10\}$. The color contours are of the temperature field at a slice through the $r-z$ plane where the images are a close-up view near the sidewall region. The black solid line represents the fluid-solid boundary. The left part is the solid sidewall region and the right part is the fluid region. For the fluid region, the color contours of the temperature field are red for hot rising fluid and blue for cold falling fluid. For the solid region red is hot and blue is cold. (a) $\beta_k = 0.1$, (b) $\beta_k = 1.0$, (c) $\beta_k = 10$.

In light of this, one can see that the deviations of the temperature profile away from the linear conduction profile, at the fluid-solid interface, are largest for Fig. 7(a). The deviations decrease as the solid sidewall becomes more conducting. In Fig. 7(c) it is clear that the linear conduction profile is present in the entire solid sidewall region.

In Fig. 8 we present a three-dimensional view illustrating the spatial variation of the sidewall heat flux with respect to the instantaneous flow field pattern that is present at a particular time t_0 . Results are shown for an insulating sidewall with $\beta_k = 0.1$ in panel (a) and for a conducting sidewall with $\beta_k = 10$ in panel (b). Overall the domain is tilted at an angle of 30° with respect to the vertical to increase the visibility of the interface between the sidewall region and the fluid. The color contours are of the temperature field at the horizontal mid-plane ($z = 1/2$) where red is hot and blue is cold. At $r = \Gamma_1$ a vertical slice of the sidewall interface is plotted with

grey-scale contours representing the local heat transfer through the sidewall $q_w(r = \Gamma_1, z, t_0)$. On this sidewall interface, light regions represent a heat flux from the sidewall into the fluid $q_w > 0$ and dark regions represent a heat flux from the fluid into the sidewall $q_w < 0$. The color scales and grey scales are the same for panels (a) and (b).

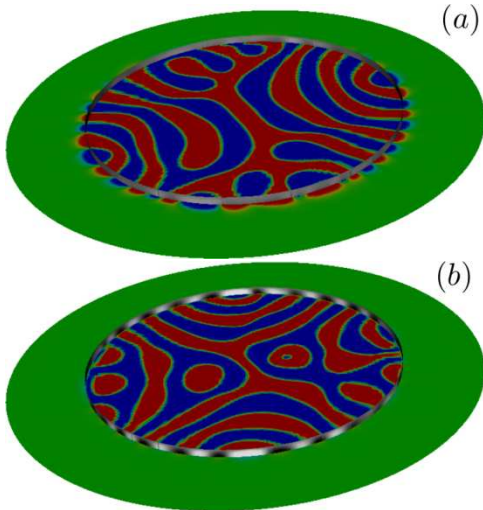


FIG. 8. (color online) A three-dimensional view of the relationship between the heat flux through the sidewalls and the flow field pattern. The color contours are of the temperature field at a mid-plane slice ($z = 1/2$). In the fluid region red is hot rising fluid and blue is cold falling fluid and in the solid sidewall region the color represents the temperature of the solid material. A vertical-slice is shown at the interface between the solid and the fluid. The heat flux through the sidewall is shown using a gray scale where light indicates regions on the sidewall where the heat flux is from the solid region into the fluid filled region and dark regions indicate where the heat flux is from the fluid filled region into the solid sidewall. Overall, the domain is tilted at an angle of 30° with respect to the vertical in order to clearly illustrate the heat flux on the sidewall interface. The color scale (-0.45 for blue, 0.55 for red) and gray scale (-0.5 for black, 0.5 for white) are the same for both panels. (a) $\beta_k = 0.1$, (b) $\beta_k = 10$.

Figure 8(a) shows results for an insulating sidewall with $\beta_k = 0.1$. Overall, there is a spatial variation in the sidewall heat flux. When the fluid near the sidewall is cool (blue) the heat flux at the sidewall is into the fluid layer (light). Similarly, when the fluid near the sidewall is hot (red) the heat flux at the sidewall is into the sidewall (dark). This is also illustrated in Fig. 8(b) where the sidewall is a good conductor $\beta_k = 10$ and the heat flux at the sidewalls is larger.

This clearly illustrates how the spatial variations of the sidewall heat flux q_w stabilizes the flow. Whenever there is a local region of fluid near the sidewall that is hot (red), the sidewall near that region will absorb heat to drive the fluid back toward the linear conduction value. At the mid-plane slice that is shown this would be a

temperature of $T_f = 1/2$ which is represented as green contours. Similarly, when the local fluid region is cold (blue) the local sidewall region will provide heat.

C. Lyapunov exponents and vectors

Next, we quantitatively probe how the presence of finite sidewalls affect the dynamics of the chaotic convection by computing the Lyapunov exponents. Figure 9(a) shows the variation of the leading order Lyapunov exponent λ_1 as a function of the thermal conductivity ratio β_k . The symbols are the results from our numerical simulations with finite sidewalls. The upper dashed line is the value of λ_1 for a perfectly insulating sidewall $\beta_k = 0$ and the lower dashed line if for a perfectly conducting sidewall $\beta_k = \infty$. For all cases $\lambda_1 > 0$ which indicates that the dynamics are chaotic as expected.

The value of λ_1 is largest for perfectly insulating sidewalls. The value of λ_1 then decreases as the conductivity of the sidewall increases and reaches a lower bound for perfectly conducting sidewalls. These trends align with our results and discussion demonstrating the stabilizing effect of conducting sidewalls.

We have also computed the spectrum of Lyapunov exponents λ_i where $i = 1, \dots, 40$ for all values of β_k that we have discussed. Using the spectrum of Lyapunov exponents we compute the fractal dimension D_λ using the Kaplan-Yorke formula given in Eq. (23). The value of the fractal dimension is an estimate for the number of chaotic degrees of freedom needed to describe the dynamics, on average [22].

Figure 9(b) shows the variation of D_λ as a function of β_k . The upper dashed line is the fractal dimension for a perfectly insulating sidewall and the lower dashed line is the fractal dimension for a perfectly conducting sidewall. The symbols are the results from our numerical simulations with finite sidewalls.

Figure 9(b) shows that the fractal dimension of the dynamics is largest for a perfectly insulating sidewall which yields a value of $D_\lambda \approx 25$. The fractal dimension decreases as the sidewall conductivity increases from zero and has a lower bounding value of $D_\lambda \approx 18.5$ for a perfectly conducting sidewall. This is a reduction of the fractal dimension by more than a quarter due to the influence of the sidewall. This provides further evidence quantifying the stabilizing effect of the sidewall heat transfer on the chaotic dynamics.

We emphasize that this stabilizing effect of the sidewall is despite the fact that the integrated amount of heat transfer through the sidewall is less than 1% of the heat transport through the fluid layer. This is evident by comparing the dashed (red) lines of Fig. 5 where $|Q_w| \lesssim 5$ with the values of $Q_b(t)$ and $|Q_t(t)|$ shown in Fig. 3 where $Q_b(t) \approx |Q_t(t)| \approx 600$. The relative influence of the sidewall boundary condition should diminish as the aspect ratio of the convection domain is increased, although this is not something we have explored further.

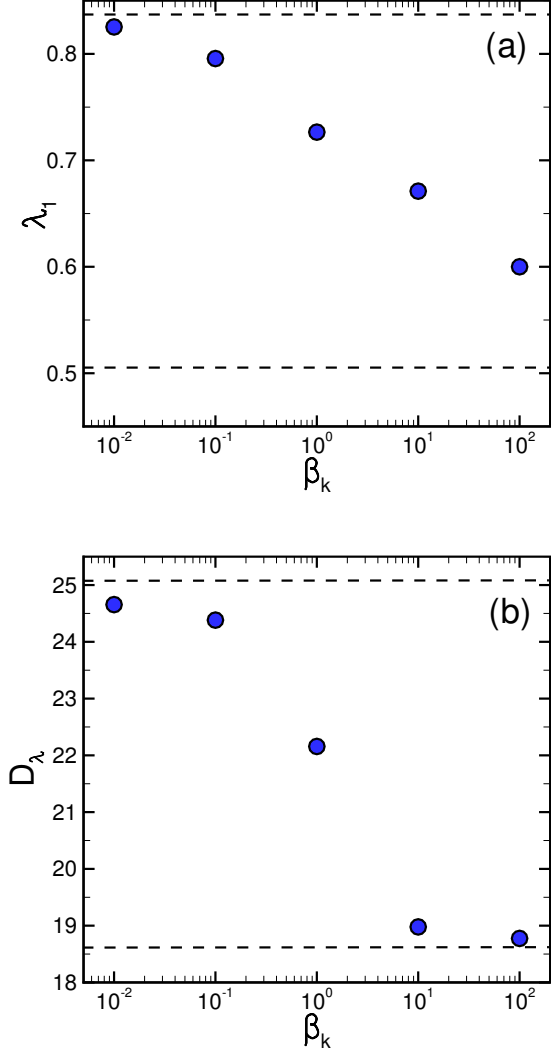


FIG. 9. (a) The variation of the leading order Lyapunov exponent λ_1 with β_k . (b) The variation of the fractal dimension D_λ with β_k . In both panels, the upper dashed line is the perfectly insulating result ($\beta_k = 0$) and the lower dashed line is the perfectly conducting result ($\beta_k = \infty$).

Further insight into the stabilizing effect of thermally conducting sidewalls can be gained by exploring the spatial variation of the leading order Lyapunov vector. Previous studies of chaotic convection have shown that the magnitude of leading order Lyapunov vector is localized near defect structures in the flow field such as roll pinch-off events, roll mergers, spiral structures, *etc.* [19, 20, 26–30]. Furthermore, it has been shown that for small to intermediate aspect ratio domains $\Gamma_1 \lesssim 10$ that the chaotic dynamics of convection are strongly influenced by the sidewalls [20]. This was demonstrated by computing the time averaged value of the leading order Lyapunov vector and showing that it is largest near the sidewalls.

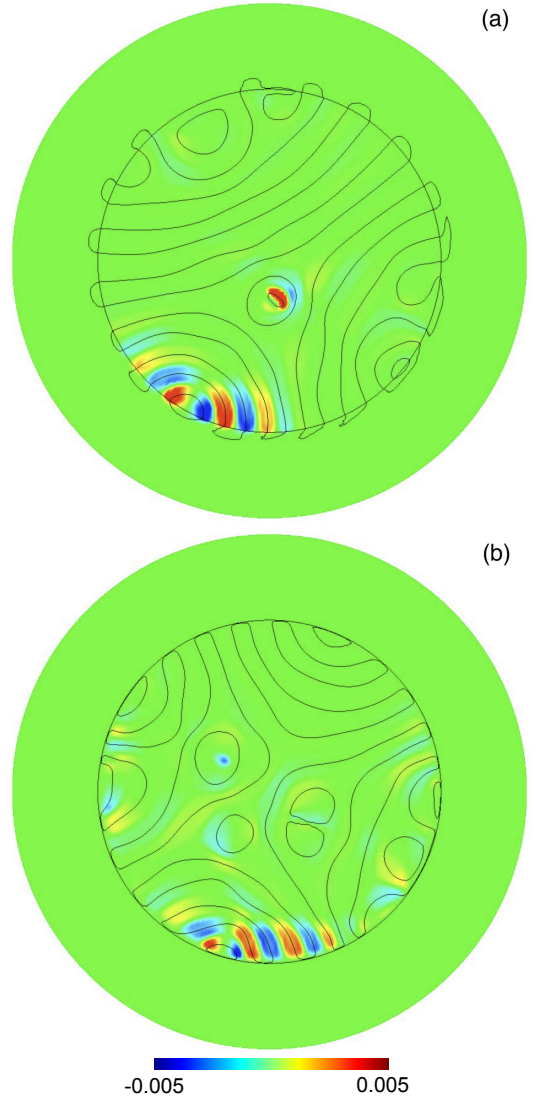


FIG. 10. The spatial variation of the leading order Lyapunov vector for (a) $\beta_k = 0.01$ and (b) $\beta_k = 100$. The color contours are of the temperature perturbation field at the horizontal mid-plane $\delta T^{(1)}(x, y, z = 1/2, t_0)$ at some instant of time t_0 . Red represents positive magnitude and blue represent negative magnitude. The black contour lines indicate the temperature contour at $T_f(x, y, z = 1/2, t_0) = T_s(x, y, z = 1/2, t_0) = 1/2$. In the fluid, this indicates the location of the convection rolls and in the solid it indicates how the temperature variation is related to the convection rolls. The black circle indicates the boundary between the fluid and solid regions and is drawn for reference.

Figure 10 illustrates the spatial variation of the leading order Lyapunov vector for a strongly insulating sidewall in panel (a) and a strongly conducting sidewall in panel (b). The Lyapunov vector is plotted by showing color contours of the temperature perturbation field at the horizontal mid-plane $\delta T^{(1)}(x, y, z = 1/2, t_0)$ at a particular time t_0 . Red represents growth with a positive

magnitude, blue represents growth with a negative magnitude, and green indicates regions with little growth. The black lines are contours of the temperature field at $T_f(x, y, z = 1/2, t_0) = T_s(x, y, z = 1/2, t_0) = 1/2$. In the fluid region these contours indicate the pattern of convection rolls and in the solid region this indicates how the temperature variation in the solid is connected with that of the flow field. The black circle at $r = \Gamma_1$ indicates the location of the boundary between the sidewall and the fluid.

Overall, in our calculations we find that the leading order Lyapunov vector is localized near small scale defect structures in the flow field with defects on the wall playing a more significant role on average. This is true for all values of the thermal conductivity ratio β_k . Figure 10 shows typical images of the spatial variation of the Lyapunov vector at a time when defect structures near the wall are important.

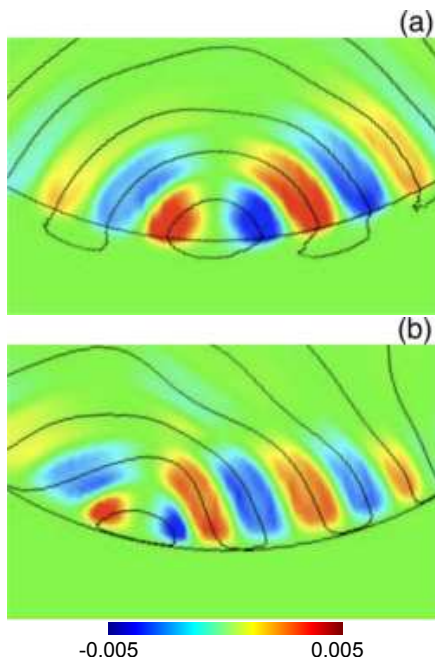


FIG. 11. A close-up view of the spatial variation of the leading order Lyapunov vector near the wall for the dynamics shown in 10 where (a) $\beta_k = 0.01$ and (b) $\beta_k = 100$. In panel (a) it is clear that the magnitude of the Lyapunov vector is large for the entire region near the sidewall. In panel (b), the Lyapunov vector nearly vanishes near the sidewall for a strongly conducting sidewall. This illustrates the stabilizing effect of conducting sidewalls.

However, we find that the spatial variation of the Lyapunov vector varies in a significant manner as a function of the sidewall boundary condition. The leading order Lyapunov vector near the sidewalls is strongly influenced by the sidewall boundary condition. Figure 11 shows a close-up of the Lyapunov vector near the sidewalls for

the conditions of Fig. 10.

In Fig. 11(a) we show a close-up view for the strongly insulating sidewall. In this case, the magnitude of the Lyapunov vector is large up to, and just beyond, the sidewall. However, in contrast, Fig. 11(b) illustrates the magnitude of the Lyapunov vector near the sidewall for strongly conducting sidewalls. In this case, the magnitude of the Lyapunov vector vanishes near the sidewalls.

This further illustrates the stabilizing influence of conducting sidewalls on the chaotic dynamics. For chaotic convection in a small to intermediately sized domain, as we explore here, the dynamics at the sidewalls contribute significantly to the dynamics. However, this is precisely where the thermal boundary condition at the sidewall is important by influencing the local fluid dynamics. As Fig. 11 shows, this results in a significant reduction in the magnitude of the Lyapunov vector near the sidewalls which is further reflected in the reduction in the fractal dimension shown in Fig. 9.

IV. CONCLUSIONS

We have explored chaotic convection in an experimentally accessible geometry with realistic sidewalls of finite size, heat capacity, and thermal conductivity. We have numerically computed the full conjugate problem by coupling the Boussinesq equations of Rayleigh-Bénard convection for the fluid dynamics with an energy equation for the temperature in the finite solid region containing the sidewall. In addition, we have computed the spectrum of Lyapunov exponents and Lyapunov vectors which allowed us to determine the fractal dimension of the dynamics and to identify spatial regions that contribute significantly to the chaos.

Our results have allowed us to quantify the stabilizing effect of thermally conducting sidewalls on chaotic dynamics. In particular, there is an interesting interplay of the heat transfer between the solid and fluid near the sidewall that always conspires to stabilize the dynamics. For small to intermediate aspect ratio convection domains, our results indicate that the sidewall boundary condition can have a significant effect upon the dynamics. These findings could also find use in applications that either want to stabilize or destabilize complex dynamics in systems far-from-equilibrium through interactions only at the bounding surfaces.

Acknowledgments: We are grateful for fruitful interactions with P. Fischer, M. Schatz, K. Mischaikow, and B. Subramanian. The research was supported by DARPA Grant No. HR0011-16-2-0033 and NSF grant no. DMS-1622299. The computations were conducted using the resources of the Advanced Research Computing center at Virginia Tech.

-
- [1] M. C. Cross and P. C. Hohenberg, “Pattern formation outside of equilibrium,” *Rev. Mod. Phys.* **65**, 851–1112 (1993).
- [2] J. P. Gollub and J. S. Langer, “Pattern formation in nonequilibrium physics,” *Rev. Mod. Phys.* **71**, S396–S403 (1999).
- [3] E. Bodenschatz, W. Pesch, and G. Ahlers, “Recent developments in Rayleigh–Bénard convection,” *Annu. Rev. Fluid Mech.* **32**, 709–778 (2000).
- [4] J. R. de Bruyn, E. Bodenschatz, S. W. Morris, D. S. Cannell, and G. Ahlers, “Apparatus for the study of Rayleigh–Bénard convection in gases under pressure,” *Rev. Sci. Instrum.* **67**, 2043–2067 (1996).
- [5] G. S. Charlson and R. L. Sani, “Thermoconvective instability in a bounded cylindrical fluid layer,” *Int. J. Heat Mass Transfer* **13**, 1479–1496 (1970).
- [6] G. S. Charlson and R. L. Sani, “On thermoconvective instability in a bounded cylindrical fluid layer,” *Int. J. Heat Mass Transfer* **14**, 2157–2160 (1971).
- [7] F. Hébert, R. Hufschmid, J. D. Scheel, and G. Ahlers, “Onset of Rayleigh–bénard convection in cylindrical containers,” *Phys. Rev. E* **81**, 046318 (2010).
- [8] J. Yu, A. Goldfaden, M. Flagstad, and J. D. Scheel, “Onset of Rayleigh–bénard convection for intermediate aspect ratio cylindrical containers,” *Phys. Fluids* **29**, 024107 (2017).
- [9] I. Catton and D. K. Edwards, “Effect of side walls on natural convection between horizontal plates heated from below,” *J. Heat Trans.* **89**, 295–299 (1967).
- [10] I. Catton, “Effect of wall conduction on the stability of a fluid in a rectangular region heated from below,” *J. Heat Trans.* **94**, 446–452 (1972).
- [11] J. C. Buell and I. Catton, “The effect of wall conduction on the stability of a fluid in a right circular cylinder heated from below,” *Journal of Heat Transf.* **105**, 255–260 (1983).
- [12] A. Ivančić, A. Oliva, C. D. Pérez Segarra, and M. Costa, “Heat transfer simulation a vertical cylindrical enclosures for supercritical Rayleigh number and arbitrary side-wall conductivity,” *Int. J. Heat Mass Transfer* **42**, 323–343 (1999).
- [13] M. R. E. Proctor, “Planform selection by finite-amplitude thermal convection between poorly conducting slabs,” *J. Fluid Mech.* **113**, 469–485 (1981).
- [14] M. R. Paul, K.-H. Chiam, M. C. Cross, P. F. Fischer, and H. S. Greenside, “Pattern formation and dynamics in Rayleigh–Bénard convection: numerical simulations of experimentally realistic geometries,” *Physica D* **184**, 114–126 (2003).
- [15] S. Chandrasekhar, *Hydrodynamic and Hydromagnetic Stability* (Dover, New York, 1961).
- [16] A. F. Mills., *Heat and Mass Transfer* (Irwin, 1995).
- [17] J. P. Eckmann and D. Ruelle, “Ergodic theory of chaos and strange attractors,” *Rev. Mod. Phys.* **57**, 617–656 (1985).
- [18] A. Wolf, J. B. Swift, H. L. Swinney, and A. Vastano, “Determining Lyapunov exponents from a time series,” *Physica D* **16**, 285–317 (1985).
- [19] M. R. Paul, M. I. Einarsson, P. F. Fischer, and M. C. Cross, “Extensive chaos in Rayleigh–Bénard convection,” *Phys. Rev. E* **75**, 045203 (2007).
- [20] A. Karimi and M. R. Paul, “Quantifying spatiotemporal chaos in Rayleigh–Bénard convection,” *Phys. Rev. E* **85**, 046201 (2012).
- [21] J. L. Kaplan and J. A. Yorke, “Lecture notes in math,” **730**, 204 (1979).
- [22] J. D. Farmer, E. Ott, and J. A. Yorke, “The dimension of chaotic attractors,” *Physica D* **7**, 153–180 (1983).
- [23] Guenter Ahlers, “Low temperature studies of the Rayleigh–Bénard instability and turbulence,” *Phys. Rev. Lett.* **33**, 1185–1188 (1974).
- [24] G. Ahlers and R. P. Behringer, “Evolution of turbulence from the Rayleigh–Bénard instability,” *Phys. Rev. Lett.* **40**, 712–716 (1978).
- [25] M. R. Paul, M. C. Cross, P. F. Fischer, and H. S. Greenside, “Power-law behavior of power spectra in low Prandtl number Rayleigh–Bénard convection,” *Phys. Rev. Lett.* **87**, 154501 (2001).
- [26] D. A. Egolf, I. V. Melnikov, W. Pesch, and R. E. Ecke, “Mechanisms of extensive spatiotemporal chaos in Rayleigh–Bénard convection,” *Nature* **404**, 733–736 (2000).
- [27] J. D. Scheel and M. C. Cross, “Lyapunov exponents for small aspect ratio Rayleigh–Bénard convection,” *Phys. Rev. E* **74**, 066301 (2006).
- [28] A. Jayaraman, J. D. Scheel, H. S. Greenside, and P. F. Fischer, “Characterization of the domain chaos convection state by the largest Lyapunov exponent,” *Phys. Rev. E* **74**, 016209 (2006).
- [29] M. Xu and M. R. Paul, “Covariant Lyapunov vectors of chaotic Rayleigh–Bénard convection,” *Phys. Rev. E* **93**, 062208 (2016).
- [30] M. Xu and M. R. Paul, “Spatiotemporal dynamics of the covariant Lyapunov vectors of chaotic convection,” *Phys. Rev. E* **97**, 032216 (2018).